

## Mechanical properties of graphene oxides

Lizhao Liu,<sup>ab</sup> Junfeng Zhang,<sup>ab</sup> Jijun Zhao<sup>\*ab</sup> and Feng Liu<sup>c</sup>

Received 11th May 2012, Accepted 27th July 2012

DOI: 10.1039/c2nr31164j

The mechanical properties, including the Young's modulus and intrinsic strength, of graphene oxides are investigated by first-principles computations. Structural models of both ordered and amorphous graphene oxides are considered and compared. For the ordered graphene oxides, the Young's modulus is found to vary from 380 to 470 GPa as the coverage of oxygen groups changes, respectively. The corresponding variations in the Young's modulus of the amorphous graphene oxides with comparable coverage are smaller at 290–430 GPa. Similarly, the ordered graphene oxides also possess higher intrinsic strength compared with the amorphous ones. As coverage increases, both the Young's modulus and intrinsic strength decrease monotonically due to the breaking of the sp<sup>2</sup> carbon network and lowering of the energetic stability for the ordered and amorphous graphene oxides. In addition, the band gap of the graphene oxide becomes narrower under uniaxial tensile strain, providing an efficient way to tune the electronic properties of graphene oxide-based materials.

### Introduction

Graphene oxide (GO), an important material used to massively synthesize graphene,<sup>1–3</sup> can be considered as graphene functionalized by oxygen-containing groups. Due to the presence of surface functional groups, GO exhibits some unique properties that are distinctly different from pristine graphene, which allow its technological applications in many fields, such as microelectronic and chemical devices,<sup>4–6</sup> energy storage<sup>7,8</sup> and composite materials.<sup>9,10</sup> Recently, numerous experimental efforts<sup>11–16</sup> have been devoted to determining the functional groups/bond types of GOs. Now it is generally accepted that GO mostly contains hydroxyl (–OH) and epoxy (–O–) groups on its basal plane.<sup>13,15</sup>

It is well-known that graphene, as a truly two-dimensional (2D) material, exhibits fascinating mechanical properties with a Young's modulus ( $E$ ) of  $\sim 1.0$  TPa and an intrinsic strength ( $\tau_c$ ) of  $130 \pm 10$  GPa,<sup>17</sup> which are promising for future nanoscale devices.<sup>18,19</sup> Since GO is the oxygen-functionalized graphene, one interesting fundamental question is how would the oxygen-containing groups affect the mechanical properties of the perfect graphene sheet. Practically, knowledge of GO's mechanical properties is of key importance for its future applications.

Early in 2007, Dikin *et al.* measured the  $E$  ( $\sim 30$  GPa in average) and  $\tau_c$  (up to  $\sim 130$  MPa) of GO sheets, depending on the water

content and thickness of the samples.<sup>20</sup> Afterwards, several groups studied the mechanical properties of GO sheets and obtained different results, varying with the sample details.<sup>21,22</sup> In general, the reported  $E$  and  $\tau_c$  values for GO sheets show a wide range of distributions of 6–42 GPa and 76–293 MPa, respectively.<sup>23</sup> Furthermore, the mechanical properties of GO sheets can be tuned by heteroatom doping or polymer compositing.<sup>23–28</sup>

When the thickness of the GO sheet is reduced down to a few layers, its Young's modulus increases dramatically to about 200 GPa.<sup>29,30</sup> Especially, monolayer GO has a much larger Young's modulus than that of a thick GO sheet. From atomic force microscopy (AFM) measurements, Gómez-Navarro *et al.* pointed out that monolayer GO has a mean  $E$  value of 250 GPa with a standard deviation of 150 GPa.<sup>31</sup> Taking the distance of 7 Å for the van der Waals (vdW) interaction between the GO layers for monolayer GO,  $E = 207.6 \pm 23.4$  GPa was reported by Suk *et al.* using AFM measurements combined with finite element analysis.<sup>30</sup>

Theoretically, using a molecular dynamics (MD) simulation technique, an  $E$  of  $\sim 670$  GPa and  $\tau_c$  of 63 GPa were obtained for GO models constructed by the Monte Carlo method, where the vdW distance of the GO layers was assumed to be 3.4 Å.<sup>32</sup> If a vdW distance of 7 Å (consistent with the interlayer vdW distance used in ref. 30) was used, the theoretical values of  $E$  and  $\tau_c$  would become  $\sim 325$  GPa and  $\sim 31$  GPa, respectively. Employing MD and molecular mechanics simulations with the COMPASS force field, Zheng *et al.* considered the effects of different functional groups on the mechanical properties of graphene sheets and indicated that the Young's modulus of the functionalized graphene sheet reduces with the increasing coverage of the surface functional groups.<sup>33</sup>

Despite the above mentioned efforts, there is still only limited knowledge about the mechanical behavior of GO from the

<sup>a</sup>Key Laboratory of Materials Modification by Laser, Ion and Electron Beams (Dalian University of Technology), Ministry of Education, Dalian 116024, China. E-mail: zhaojj@dut.edu.cn; Tel: +86-411-84706100

<sup>b</sup>College of Advanced Science and Technology, Dalian University of Technology, 116024 Dalian, China

<sup>c</sup>Department of Materials Science and Engineering, University of Utah, Salt Lake City, Utah 84112, USA

theoretical point of view; in particular, no accurate first-principles results have been reported to our knowledge. Most importantly, the dependence of the mechanical properties on the surface coverage, type and arrangement (*e.g.*, ordered *versus* amorphous) of the functional groups of GO remains unknown. To address these critical issues, here we systematically investigate the mechanical properties of both ordered and amorphous GOs of different oxidation coverages using density functional theory (DFT) calculations. We found that the key mechanical parameters ( $E$  and  $\tau_c$ ) of the GOs generally decrease with increasing coverage of the functional groups. The ordered GO always possess larger  $E$  and  $\tau_c$  than the amorphous GO at the same coverage. In addition, the electronic properties of the GO materials can be tuned by uniaxial tensile strain.

## Structural models and computational methods

### GO models

The atomic structures of GOs are rather complicated and remain a subject under debate. There are many experimental evidences indicating that GOs are amorphous,<sup>11,12,15</sup> but theoretical investigations suggest that the ordered structural models are thermodynamically favourable.<sup>7,34–36</sup> Considering the discrepancy between the experiments and theories, both ordered and amorphous structural models of the GOs are considered here, which were carefully examined in our previous work.<sup>37</sup> We first defined the coverage of the functional groups ( $R$ ) as:

$$R = \text{number of } sp^3 \text{ C (bonded with } -\text{O- or } -\text{OH}) / \text{total number of C atoms} \times 100\%. \quad (1)$$

Assuming an OH/O ratio of 2.00, within the range of 1.06–3.25 from the experimental observations,<sup>38</sup> different ordered GO structures with a series of  $R = 10\%$ , 20%, 33%, 40%, 50% and 67% were studied, which were constructed by expanding the width of the supercell with the inclusion of only one  $\text{h}_2\text{e}_2^1$  chain.<sup>35</sup> Similarly, fixing an OH/O ratio of 2.00, amorphous GO models with  $R = 10\%$ , 20%, 30%, 40%, 50%, 60% and 70% were constructed by randomly placing epoxide and hydroxyl groups on a graphene supercell with 80 carbon atoms following some structural rules.<sup>37</sup> Note that we only considered the epoxide and hydroxyl groups since the structural models studied here are periodic systems without holes or edges. This is based on the previous experimental demonstration that GO bears hydroxyl and epoxy groups mostly on its basal plane.<sup>13,15</sup>

Actually, an amorphous GO at a fixed  $R$  can have different OH/O ratios. To examine this effect, amorphous GOs with  $R = 50\%$  but different OH/O ratios (OH/O = 0.22, 0.50, 0.86, 1.33, 2.00, 3.00, 4.67 and 8.00) were also studied. Fig. 1 shows the atomic structures of the ordered and amorphous GOs, as well as the direction of the uniaxial tensile strain applied in our study.

### Computational methods

Periodic first-principles computations were performed using the plane-wave pseudopotential technique as implemented in the Vienna *ab initio* simulation package (VASP)<sup>39</sup> with the PW91

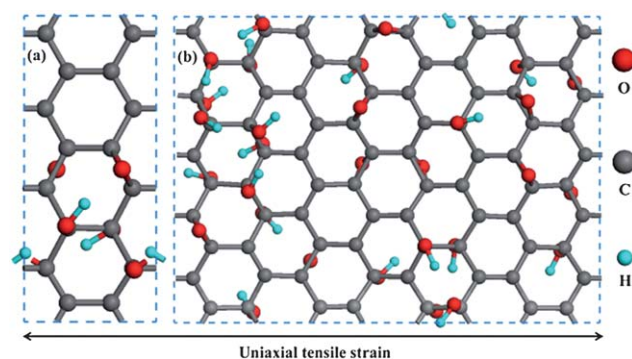


**Fig. 1** Representative structural models of GOs with OH/O = 2.00 and  $R = 50\%$ , where (a) is the ordered GO and (b) is the amorphous one. The large red balls are oxygen, the medium gray balls are carbon, and the small light blue balls are hydrogen, respectively.

functional<sup>40</sup> for the exchange–correlation interaction and the PAW pseudopotential<sup>41,42</sup> for ion–electron interactions. A kinetic energy cutoff value of 800 eV was adopted to ensure good convergence of the stresses. During the geometry optimization, the  $k$  space for amorphous GO systems of a large supercell was sampled by the  $\Gamma$  point, and Monkhorst–Pack grids<sup>43</sup> with a separation of  $0.03 \text{ \AA}^{-1}$  were chosen for the small ordered GO supercell structures with different sizes. The supercell dimension perpendicular to the GO plane is chosen to be  $15 \text{ \AA}$  to avoid the interaction between the GO layer and its periodic images. All geometric structures were fully relaxed using the conjugate gradient algorithm until the force on each atom was smaller than  $0.01 \text{ eV \AA}^{-1}$ .

Before calculating mechanical properties, each structural model was fully relaxed to its equilibrium state by minimizing the force on the atoms and the stress on the supercell. Starting from the equilibrium supercell lattice length ( $L_0$ ), we elongated the GOs with a uniaxial strain step of 0.5% up to a maximum strain of 2% to compute the Young's Modulus  $E$ , which is defined by the formula below:

$$E = \frac{Z_0}{d_0} \times \frac{\sigma}{\varepsilon} = \frac{15}{7} \times \frac{\sigma}{\varepsilon} = 2.14 \frac{\sigma}{\varepsilon}, \quad (2)$$

where  $Z_0 = 15 \text{ \AA}$  is the supercell dimension perpendicular to the GO plane,  $d_0 = 7 \text{ \AA}$  is the vdW distance between GO sheets, as reported in ref. 30,  $\sigma$  is the stress and  $\varepsilon = (L - L_0)/L_0$  is the strain, respectively.

## Results and discussion

### Young's modulus $E$

**OH/O = 2.00 with various coverages.** We first discuss both ordered and amorphous GOs with OH/O = 2.00 but different coverages. The Young's modulus for these GO models as a function of oxidation coverage is plotted in Fig. 2. Generally speaking, as the  $R$  changes,  $E$  varies from 380 to 470 GPa for the ordered GOs, and from 290 to 430 GPa for the amorphous GOs, respectively. These results agree well with the measured values of  $E = 250 \pm 150 \text{ GPa}$ <sup>30,31</sup> as well as the theoretical value  $E$  of  $\sim 325 \text{ GPa}$  from empirical MD simulations with an interlayer vdW distance of  $7 \text{ \AA}$ .<sup>32</sup>

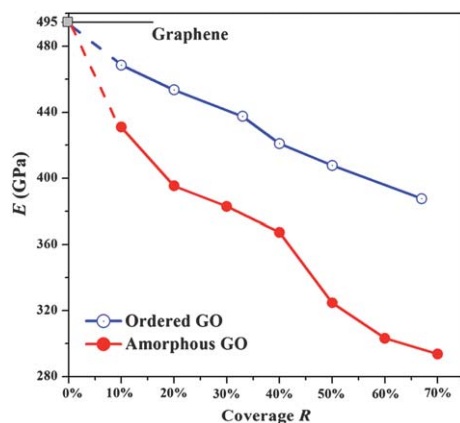


**Fig. 2**  $E$  as a function of  $R$  for both ordered and amorphous GOs is presented. The scaled values for a perfect graphene sheet by assuming a vdW distance of 7 Å (filled square) are given for reference.

As the coverage increases, the Young's modulus decreases monotonically due to the incremental breaking of the perfect  $sp^2$  carbon network. This trend is also consistent with the previous report that the Young's modulus decreases as the coverage of functional groups on the graphene sheet increases.<sup>33</sup> In addition, the ordered GO has a higher  $E$  than the amorphous GO with the same  $R$  because the former is energetically more stable.<sup>37</sup> For reference, the mechanical properties of the perfect graphene were also calculated. Taking a vdW distance of 3.34 Å,<sup>44,45</sup> the  $E$  for the graphene was found to be 1037 GPa, in good agreement with the experimental value ( $E$  of  $\sim 1.0$  TPa) measured by Lee *et al.*<sup>17</sup> To directly compare with the GO systems, we could assume an interlayer vdW distance of 7 Å, and then the  $E$  of the graphene is re-scaled to 495 GPa, which should represent the upper limits of GOs with very low coverage (see Fig. 2). In short, GO monolayers inherit the excellent mechanical properties of the pristine graphene, with a moderate downgrade due to some local disruption of the  $sp^2$  carbon network by surface functional groups.

### $R = 50\%$ with varying OH/O ratios

To examine the effect of OH/O ratio, the mechanical properties of amorphous GOs with  $R = 50\%$  but different OH/O ratios were

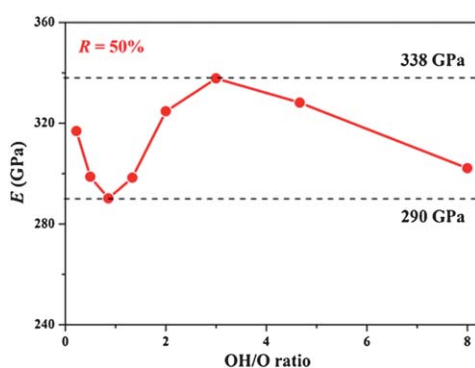


**Fig. 3** Relationship between  $E$  and OH/O ratio for the amorphous GO structures with  $R = 50\%$  are plotted. The dashed lines bracket the range of  $E$  values.

investigated. As presented in Fig. 3,  $E$  fluctuates between 290 GPa and 338 GPa as the OH/O ratio varies. In other words, the effect of the OH/O ratio on the mechanical properties of the amorphous GOs is less significant than that of the  $R$ . To further confirm this fluctuating effect, we also studied the case of  $R = 20\%$  with different OH/O ratios. It was found that for the amorphous GOs with  $R = 20\%$  and OH/O = 0.29, 0.67, 1.20, 2.00, 3.33 and 6.00,  $E$  has a range of  $390 \pm 14$  GPa. The main reason is that once  $R$  is fixed, the percentage of  $sp^3$  carbon atoms remains nearly constant; thus, changing the OH/O ratio at a given integrity of  $sp^2$  network only weakly affects the stability of the 2D graphene-based sheet. Again, this result indicates that the disruption of the  $sp^2$  carbon network by local  $sp^3$  rehybridization due to functional groups is the major factor for determining the mechanical properties of the GO monolayers.

As shown in Fig. 3, the computed Young's modulus reaches its minimum (290 GPa) and maximum (338 GPa) at an OH/O ratio of 0.86 and 3.00, respectively. To understand the origin of such a variation we present these two GO structures in Fig. 4. Obviously, the GO structure with OH/O = 0.86 is more wrinkled in geometry than the one with OH/O = 3.00. As reported by Gómez-Navarro *et al.*, the mechanical properties of GO monolayers depend on the geometry of the samples, and  $E$  is inversely proportional to the cube height of the monolayer.<sup>31</sup> Therefore, the lower  $E$  obtained for GO with OH/O = 0.86 in comparison to that with OH/O = 3.00 can be roughly interpreted by its larger height variation, which leads to a larger effective thickness. Moreover, our recent study on the mechanical properties of the graphene boundary revealed that its intrinsic strength is related to the inflection angle.<sup>45</sup> As the inflection angle increases (*i.e.*, more wrinkled in geometry), the intrinsic strength decreases linearly. Considering that the thermodynamic stability of the GO sheet increases as the OH/O ratio increases<sup>37</sup> and the height of the GO sheet fluctuates with the OH/O ratios, the observed fluctuations in  $E$  in Fig. 3 might be a compromise between the stability and the effective thickness.

### Intrinsic strength $\tau_c$ and fracture behaviour

In addition to the  $E$  calculated within a small strain regime ( $\epsilon \leq 2\%$ ), strain–stress curves up to an  $\epsilon$  of  $\sim 20\%$  for the ordered

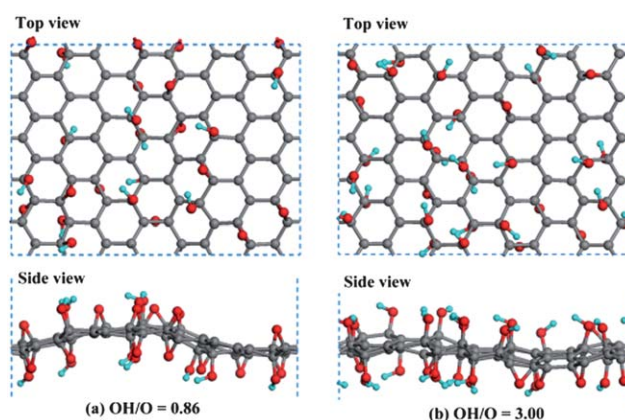


**Fig. 4** Atomic structures of amorphous GOs with  $R = 50\%$  and OH/O = 0.86 and 3.00, respectively.

and an  $\varepsilon$  of  $\sim 15\%$  for the amorphous GO structures were also calculated, as plotted in Fig. 5. Starting from the equilibrium structures, ordered GOs with OH/O = 2.00 and  $R = 10\%$ , 20%, 40% and 50% were uniaxially elongated with a tensile strain step of  $\leq 1\%$  until the fracture strain ( $\varepsilon_c$ ), which is defined by the critical strain where the strain–stress curve starts to drop, is reached (see Fig. 5(a)). For comparison, strain–stress curves of the amorphous GOs with corresponding  $R$  were also plotted in Fig. 5(b), obtained by elongating the amorphous GOs in the same way. For each GO system, its intrinsic strength  $\tau_c$  at the critical fracture strain  $\varepsilon_c$  was determined from the strain–stress curve. The theoretical results are summarized in Table 1.

First of all, it can be seen that both the  $\tau_c$  and  $\varepsilon_c$  of the ordered GOs are higher than that of the amorphous GOs at the same  $R$  because the ordered GOs are thermodynamically more stable.<sup>37</sup> For either ordered or amorphous GO structures,  $\tau_c$  decreases with the increasing  $R$ , because of the breaking of the  $sp^2$  carbon network and lowering of the stability. For comparison, the  $\tau_c$  and  $\varepsilon_c$  of a pristine graphene sheet were also calculated, corresponding to  $R = 0\%$  in Table 1. Taking  $d_0 = 3.34 \text{ \AA}$ , the  $\tau_c$  of graphene is 100.1 GPa, in accordance with the reported value of  $\sim 130$  GPa.<sup>17,45</sup> To directly compare with the GO systems, we assumed an interlayer vdW distance of  $7 \text{ \AA}$  and the  $\tau_c$  of graphene was rescaled to 47.8 GPa, which is only slightly higher than those of ordered GO with low coverage. Again, the present results indicate that GO monolayers possess excellent intrinsic strength comparable to the pristine graphene. In addition, the intrinsic strength for the GO models obtained here is also comparable to that of previous empirical MD predictions,<sup>32</sup> which gives the  $\tau_c$  of  $\sim 31$  GPa with an assumed vdW distance of  $7 \text{ \AA}$ .

Below, we further discuss the fracture behaviours of the GOs. Taking the ordered GOs as examples, the first fractured bond is always an  $sp^3$  hybridization C–C bond for all the ordered GO systems considered, as highlighted in blue in Fig. 6. This phenomenon can be explained by the following two points. Firstly, the carbon atom bonded with a hydroxyl group has a larger bond angle ( $\sim 105^\circ$ ) than that bonded with an epoxide group ( $\sim 55^\circ$ ), which is closer to that of the ideal  $sp^3$  hybridization state ( $109.47^\circ$ ).<sup>37</sup> Secondly, compared with its neighbouring C–C bonds, the highlighted C–C bond is far away from the chained epoxide groups. Thus the hydroxyl groups on its neighbouring C–C bond can bond with the epoxide groups to form hydrogen bonds. The formation of hydrogen bonds would further shorten

**Table 1** The intrinsic strength  $\tau_c$  and critical failure strain  $\varepsilon_c$  of the ordered and amorphous GOs with different  $R$  are listed, along with that of the pristine graphene ( $R = 0\%$ ) for comparison

$R$	$\tau_c$ (GPa)		$\varepsilon_c$ (%)	
	Ordered GOs	Amorphous GOs	Ordered GOs	Amorphous GOs
0%	47.8		20%	
10%	46.3	40.9	18%	13%
20%	44.4	37.5	17%	13%
40%	40.0	33.1	16%	13%
50%	38.6	27.9	16%	10%

the C–C bond. These two factors mean that the highlighted C–C bond has a larger bond length than the others, making it fracture first during elongation. As for the amorphous GOs, due to the complexity of the structures, amorphous GOs with different  $R$  values exhibit different failure behaviours. The first fractured bond depends on the structural details of the amorphous GOs.

### Effect of tensile strain on the electronic properties

As reported before, GO has a theoretical LDA band gap ranging from a few tenths of an eV to 4 eV, depending on the oxidation coverage and the location of the oxidized region.<sup>34</sup> Its electronic properties are also expected to change under uniaxial tensile strain. Taking an ordered GO structure with OH/O = 2.00 and  $R = 50\%$  and an amorphous one with the same OH/O and  $R$  as examples, we investigated their electronic properties during elastic elongation. The elastic strain limit is 11% for the ordered GO and 8% for the amorphous GO, respectively. In Fig. 7, the electron densities of states for the GOs under uniaxial tensile strain within the elastic region are plotted. When the GO sheets are uniaxially elongated from the equilibrium states, the gaps become narrower, implying a trend of metallization. For the ordered GO, the gap dramatically decreases by more than 50% as the GO is elongated by 10%. Meanwhile, the gap variation is less pronounced for the amorphous GO, decreasing by  $\sim 23\%$  after 8% elongation. In the cases of amorphous GOs, the defect-induced mid-states among the forbidden band region were ignored. As reported before,<sup>37</sup> the mid-states may originate from unsaturated dangling bonds, structural distortion and locally residual  $sp^2$  and

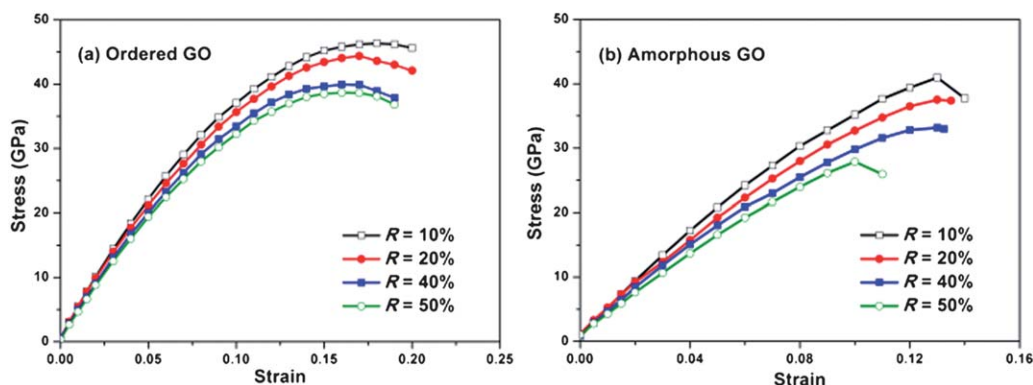


**Fig. 5** Strain–stress curves for both the ordered (a) and amorphous (b) GO structures as functions of  $R$ .

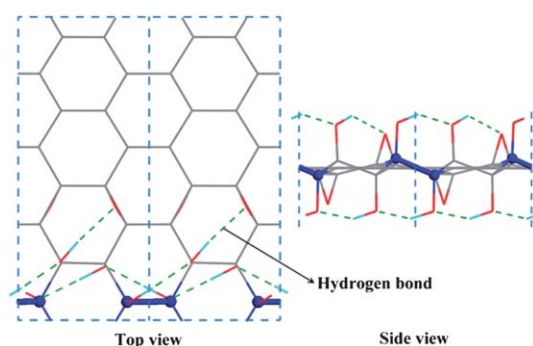


**Fig. 6** Fracture behaviour of the ordered GO with OH/O = 2.00 and  $R = 50\%$ . The first fractured C–C bond is highlighted in blue and thick stick.

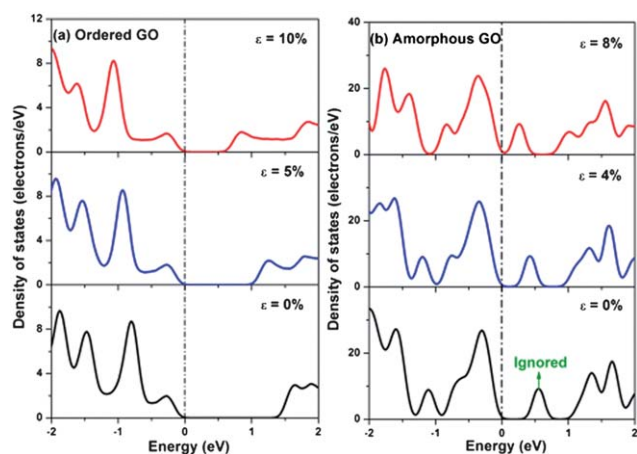


**Fig. 7** Electron density of states as a function of tensile strain for the ordered (a) and amorphous (b) GOs both with OH/O = 2.00 and  $R = 50\%$ . The zero energy is set at the last occupied state.

$sp^2$ – $sp^3$  bonds, which may trap the electrons and have no contributions to the electrical conductivity in real material applications.<sup>46</sup> Moreover, this trapping effect of defective states and the trend of band gap *versus* coverage rate have been reported in previous experimental measurements,<sup>47</sup> supporting the feasibility of ignoring the defect-induced mid-states here.

In a simple general picture, the strain-induced shrinkage of the band gap can be understood as follows. Consider a diatomic molecule, if its bond length is increased by the tensile strain, its HOMO–LUMO gap increases due to the reduced molecular orbital overlap (or interatomic hopping in the tight-binding picture). Conversely, its HOMO–LUMO gap decreases under compressive strain. Similarly, for bulk materials, the band gap generally decreases (increases) under hydrostatic compressive tensile strain when the crystal symmetry is conserved. However, the situation is different and more complex under uniaxial or biaxial strain in that the band gap may decrease under either compressive or tensile strain, because the crystal symmetry breaks under uniaxial/biaxial strain and the broken symmetry lifts the degeneracy of the band edge states, always causing a decrease of the band gap. For example, for the well-known case of the Si band under strain,<sup>48,49</sup> the six-fold degenerate conduction band minima split into two subsets of  $\Delta_2$  and  $\Delta_4$

bands under biaxial strain. When the gap associated with the  $\Delta_4$  band edges increases with the increasing “tensile” biaxial strain in the  $x$ – $y$  plane, the gap associated with the  $\Delta_2$  band edges will increase with the increasing “compressive” uniaxial strain in the  $z$ -direction perpendicular to the  $x$ – $y$  plane due to the Poisson effect.<sup>48,49</sup> Consequently, counting all the band-edge states the overall band gap always decreases under either compressive or tensile biaxial strain because one subset of bands are always under compressive strain due to the Poisson effect. For the ordered GO studied here, the band structures under tensile strain are shown in Fig. 8. In the valence band region, it can be seen that one energy band (highlighted in red) becomes lower and flatter during the tensile strain compared with its initial state. With the lowering of this band, another band crossed with it (highlighted in green) is lifted up due to the breaking of lattice symmetry, causing a rise of the valence band. Similarly, the corresponding antibonding bands in the conduction band region are also split, resulting in a degradation of the conduction band. These two factors account for the decrease of the band gap under tensile strain. To gain further insight into the band structures, we analysed the orbital corresponding to the energy band highlighted in red. As presented in the bottom of Fig. 8, the highlighted energy bands correspond to C–O hybridized molecular levels. As the GO is uniaxially elongated, C–O hybridization becomes weaker and more electrons are released, causing a reduction of the overall band gap.

Furthermore, we plotted the variation of the band gaps under uniaxial tensile strain in Fig. 9. When the ordered GO is elongated within the elastic region, the band gap decreases linearly with the increasing tensile strain. Compared with the ordered GO, the band gap decreases more slowly for the amorphous GO. In other words, the ordered GO has a wider range of gap tenability than the amorphous GO by applying uniaxial strain. In addition, it is well-known that conventional DFT calculations usually underestimate the band gap. Thus the true band gaps of the GO materials should be even larger, but the trend of changing gap under strain would still be quantitatively reliable.

As shown in previous studies, tunable band gaps of chemically derived GOs allow their promising performance in electronics and optoelectronics.<sup>50–52</sup> Through appropriately tuning the deposition and reduction parameters, the GO films can be made insulating, semiconducting, or semimetallic, while maintaining optical transparency.<sup>53</sup> This enables the GO films to be transparent and conducting electrodes for optoelectronic devices.<sup>54,55</sup> In addition, the optical transmittance of GO films

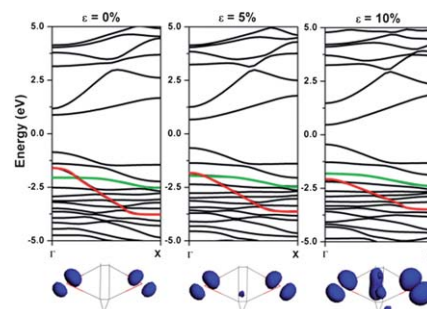


**Fig. 8** Band structures and orbital variation of the ordered GO under tensile strain with OH/O = 2.00 and  $R = 50\%$ .

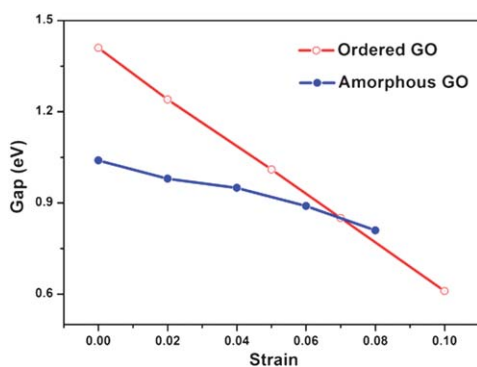


**Fig. 9** Relationship of the band gap under uniaxial tensile strain for the ordered and amorphous GOs both with OH/O = 2.00 and  $R = 50\%$ .

can be continuously tuned by varying the film thickness or the extent of reduction.<sup>5</sup> In particular, GO with a tunable band gap could present excellent nonlinear optical properties,<sup>56</sup> better than that of the  $C_{60}$  and single-walled carbon nanotubes.<sup>57</sup> Therefore, the present finding of continuous engineering of the band gaps of GO materials throughout the visible region by tensile strain may offer new opportunities for the application of GOs in electronic and optoelectronic devices.

## Conclusions

The mechanical properties of both the ordered and amorphous GOs were systematically studied. The ordered GOs possess a higher Young's modulus and intrinsic strength than the amorphous GOs with the same coverage of the functional groups because the ordered GOs are more energetically stable. Both ordered and amorphous GOs inherit the excellent mechanical properties of the pristine graphene, while the mechanical parameters (Young's modulus and intrinsic strength) decrease moderately with increasing the coverage due to the disturbance by  $sp^3$  carbons. In general, mechanical properties of GOs depend mainly on the surface coverage and arrangement (ordered or amorphous). The detail ratios of the functional groups have little effect on the mechanical properties. Investigation of the electromechanical effects indicated that the electronic properties can be tuned by the uniaxial tensile strain. As the GO is elongated, its gap becomes narrower due to weakening of C–O hybridization. The present theoretical results shed some light on the mechanical behaviours and electromechanical effects of the GOs, which are useful for the future applications of the GO-based materials.

## Acknowledgements

This work was supported in China by the Program for Changjiang Scholars and Innovative Research Team in the University of China, Fundamental Research Funds for the Central Universities of China (no. DUT12YQ05), Fundamental Research Funds for Dalian University of Technology (no. DUT11RC(3)46) and China Postdoctoral Science Foundation (no. 2012M510795). Feng Liu acknowledges support from US DOE-BES (no. DE-FG02-04ER46027).

## Notes and references

- S. Park and R. S. Ruoff, *Nat. Nanotechnol.*, 2009, **4**, 217–224.
- M. J. Allen, V. C. Tung and R. B. Kaner, *Chem. Rev.*, 2010, **110**, 132–145.
- D. R. Dreyer, S. Park, C. W. Bielawski and R. S. Ruoff, *Chem. Soc. Rev.*, 2010, **39**, 228–240.
- C. Gómez-Navarro, R. T. Weitz, A. M. Bittner, M. Scolari, A. Mews, M. Burghard and K. Kern, *Nano Lett.*, 2007, **7**, 3499–3503.
- G. Eda, G. Fanchini and M. Chhowalla, *Nat. Nanotechnol.*, 2008, **3**, 270–274.
- J. D. Fowler, M. J. Allen, V. C. Tung, Y. Yang, R. B. Kaner and B. H. Weiller, *ACS Nano*, 2009, **3**, 301–306.
- L. Wang, K. Lee, Y. Y. Sun, M. Lucking, Z. F. Chen, J. J. Zhao and S. B. B. Zhang, *ACS Nano*, 2009, **3**, 2995–3000.
- J. Xu, K. Wang, S.-Z. Zu, B.-H. Han and Z. Wei, *ACS Nano*, 2010, **4**, 5019–5026.
- S. Stankovich, D. A. Dikin, G. H. B. Dommett, K. M. Kohlhaas, E. J. Zimney, E. A. Stach, R. D. Piner, S. T. Nguyen and R. S. Ruoff, *Nature*, 2006, **442**, 282–286.
- T. Ramanathan, A. A. Abdala, S. Stankovich, D. A. Dikin, M. Herrera Alonso, R. D. Piner, D. H. Adamson, H. C. Schniepp, X. Chen, R. S. Ruoff, S. T. Nguyen, I. A. Aksay, R. K. Prud'Homme and L. C. Brinson, *Nat. Nanotechnol.*, 2008, **3**, 327–331.
- T. Szabó, O. Berkesi, P. Forgó, K. Josepovits, Y. Sanakis, D. Petridis and I. Dékány, *Chem. Mater.*, 2006, **18**, 2740–2749.
- S. Stankovich, D. A. Dikin, R. D. Piner, K. A. Kohlhaas, A. Kleinhammes, Y. Jia, Y. Wu, S. T. Nguyen and R. S. Ruoff, *Carbon*, 2007, **45**, 1558–1565.
- W. W. Cai, R. D. Piner, F. J. Stadermann, S. Park, M. A. Shaibat, Y. Ishii, D. X. Yang, A. Velamakanni, S. J. An, M. Stoller, J. H. An, D. M. Chen and R. S. Ruoff, *Science*, 2008, **321**, 1815–1817.
- H. K. Jeong, Y. P. Lee, R. Lahaye, M. H. Park, K. H. An, I. J. Kim, C. W. Yang, C. Y. Park, R. S. Ruoff and Y. H. Lee, *J. Am. Chem. Soc.*, 2008, **130**, 1362–1366.
- W. Gao, L. B. Alemany, L. J. Ci and P. M. Ajayan, *Nat. Chem.*, 2009, **1**, 403–408.
- D. Yang, A. Velamakanni, G. Bozoklu, S. Park, M. Stoller, R. D. Piner, S. Stankovich, I. Jung, D. A. Field, C. A. Ventrice and R. S. Ruoff, *Carbon*, 2009, **47**, 145–152.
- C. Lee, X. Wei, J. W. Kysar and J. Hone, *Science*, 2008, **321**, 385–388.
- C. Chen, S. Rosenblatt, K. I. Bolotin, W. Kalb, P. Kim, I. Kymissis, H. L. Stormer, T. F. Heinz and J. Hone, *Nat. Nanotechnol.*, 2009, **4**, 861–867.
- K. S. Kim, Y. Zhao, H. Jang, S. Y. Lee, J. M. Kim, K. S. Kim, J.-H. Ahn, P. Kim, J.-Y. Choi and B. H. Hong, *Nature*, 2009, **457**, 706–710.
- D. A. Dikin, S. Stankovich, E. J. Zimney, R. D. Piner, G. H. B. Dommett, G. Evmenenko, S. T. Nguyen and R. S. Ruoff, *Nature*, 2007, **448**, 457–460.
- H. Chen, M. B. Müller, K. J. Gilmore, G. G. Wallace and D. Li, *Adv. Mater.*, 2008, **20**, 3557–3561.
- C. Chen, Q.-H. Yang, Y. Yang, W. Lv, Y. Wen, P.-X. Hou, M. Wang and H.-M. Cheng, *Adv. Mater.*, 2009, **21**, 3007–3011.
- Y. Gao, L.-Q. Liu, S.-Z. Zu, K. Peng, D. Zhou, B.-H. Han and Z. Zhang, *ACS Nano*, 2011, **5**, 2134–2141.
- S. Park, K.-S. Lee, G. Bozoklu, W. Cai, S. T. Nguyen and R. S. Ruoff, *ACS Nano*, 2008, **2**, 572–578.
- J. Liang, Y. Huang, L. Zhang, Y. Wang, Y. Ma, T. Guo and Y. Chen, *Adv. Funct. Mater.*, 2009, **19**, 2297–2302.
- S. Park, D. A. Dikin, S. T. Nguyen and R. S. Ruoff, *J. Phys. Chem. C*, 2009, **113**, 15801–15804.
- L. Zhang, Z. Wang, C. Xu, Y. Li, J. Gao, W. Wang and Y. Liu, *J. Mater. Chem.*, 2011, **21**, 10399–10406.
- O. C. Compton, S. W. Cranford, K. W. Putz, Z. An, L. C. Brinson, M. J. Buehler and S. T. Nguyen, *ACS Nano*, 2012, **6**, 2008–2019.
- J. T. Robinson, M. Zhalalutdinov, J. W. Baldwin, E. S. Snow, Z. Wei, P. Sheehan and B. H. Houston, *Nano Lett.*, 2008, **8**, 3441–3445.
- J. W. Suk, R. D. Piner, J. An and R. S. Ruoff, *ACS Nano*, 2010, **4**, 6557–6564.
- C. Gómez-Navarro, M. Burghard and K. Kern, *Nano Lett.*, 2008, **8**, 2045–2049.
- J. T. Paci, T. Belytschko and G. C. Schatz, *J. Phys. Chem. C*, 2007, **111**, 18099–18111.

- 33 Q. Zheng, Y. Geng, S. Wang, Z. Li and J.-K. Kim, *Carbon*, 2010, **48**, 4315–4322.
- 34 J. A. Yan, L. D. Xian and M. Y. Chou, *Phys. Rev. Lett.*, 2009, **103**, 086802.
- 35 L. Wang, Y. Y. Sun, K. Lee, D. West, Z. F. Chen, J. J. Zhao and S. B. Zhang, *Phys. Rev. B: Condens. Matter Mater. Phys.*, 2010, **82**, 161406.
- 36 J. A. Yan and M. Y. Chou, *Phys. Rev. B: Condens. Matter Mater. Phys.*, 2010, **82**, 125403.
- 37 L. Liu, L. Wang, J. Gao, J. Zhao, X. Gao and Z. Chen, *Carbon*, 2012, **50**, 1690–1698.
- 38 A. Buchsteiner, A. Lerf and J. Pieper, *J. Phys. Chem. B*, 2006, **110**, 22328–22338.
- 39 G. Kresse and J. Furthmüller, *Phys. Rev. B: Condens. Matter*, 1996, **54**, 11169–11186.
- 40 J. P. Perdew, K. Burke and M. Ernzerhof, *Phys. Rev. Lett.*, 1996, **77**, 3865.
- 41 P. E. Blöchl, *Phys. Rev. B: Condens. Matter*, 1994, **50**, 17953–17979.
- 42 G. Kresse and D. Joubert, *Phys. Rev. B: Condens. Matter Mater. Phys.*, 1999, **59**, 1758–1775.
- 43 H. J. Monkhorst and J. D. Pack, *Phys. Rev. B: Solid State*, 1976, **13**, 5188.
- 44 F. Liu, P. Ming and J. Li, *Phys. Rev. B: Condens. Matter Mater. Phys.*, 2007, **76**, 064120.
- 45 J. Zhang, J. Zhao and J. Lu, *ACS Nano*, 2012, **6**, 2704–2711.
- 46 H. Belgacem and A. Merazga, *Solid-State Electron.*, 2008, **52**, 73–77.
- 47 H. Chang, Z. Sun, Q. Yuan, F. Ding, X. Tao, F. Yan and Z. Zheng, *Adv. Mater.*, 2010, **22**, 4872–4876.
- 48 D. Yu, Y. Zhang and F. Liu, *Phys. Rev. B: Condens. Matter Mater. Phys.*, 2008, **78**, 245204.
- 49 Z. Liu, J. Wu, W. Duan, M. G. Lagally and F. Liu, *Phys. Rev. Lett.*, 2010, **105**, 016802.
- 50 G. Eda and M. Chhowalla, *Adv. Mater.*, 2010, **22**, 2392–2415.
- 51 K. P. Loh, Q. Bao, G. Eda and M. Chhowalla, *Nat. Chem.*, 2010, **2**, 1015–1024.
- 52 I. P. Murray, S. J. Lou, L. J. Cote, S. Loser, C. J. Kadleck, T. Xu, J. M. Szarko, B. S. Rolczynski, J. E. Johns, J. Huang, L. Yu, L. X. Chen, T. J. Marks and M. C. Hersam, *J. Phys. Chem. Lett.*, 2011, **2**, 3006–3012.
- 53 G. Eda, C. Mattevi, H. Yamaguchi, H. Kim and M. Chhowalla, *J. Phys. Chem. C*, 2009, **113**, 15768–15771.
- 54 Q. He, S. Wu, S. Gao, X. Cao, Z. Yin, H. Li, P. Chen and H. Zhang, *ACS Nano*, 2011, **5**, 5038–5044.
- 55 Z. Yin, S. Sun, T. Salim, S. Wu, X. Huang, Q. He, Y. M. Lam and H. Zhang, *ACS Nano*, 2010, **4**, 5263–5268.
- 56 Y. Zhou, Q. Bao, L. A. L. Tang, Y. Zhong and K. P. Loh, *Chem. Mater.*, 2009, **21**, 2950–2956.
- 57 Z. Liu, Y. Wang, X. Zhang, Y. Xu, Y. Chen and J. Tian, *Appl. Phys. Lett.*, 2009, **94**, 021902–021903.